Title

The Composition of Plasma inside Geostationary Orbit Based on Van Allen Probes Observations

Journal

JOURNAL OF GEOPHYSICAL RESEARCH-SPACE PHYSICS, 123(8)

ISSN

2169-9380

Authors

Yue, Chao
Bortnik, Jacob
Li, Wen
et al.

Publication Date

2018

DOI

10.1029/2018JA025344

Peer reviewed

Journal of Geophysical Research: Space Physics

RESEARCH ARTICLE
10.1029/2018JA025344

The Composition of Plasma inside Geostationary Orbit Based on Van Allen Probes Observations

Chao Yue[1], Jacob Bortnik[1], Wen Li[2], Qianli Ma[1,2], Matina Gkioulidou[3], Geoffrey D. Reeves[4,5], Chih-Ping Wang[1], Richard M. Thorne[1], Anthony T. Y. Lui[3], Andrew J. Gerrard[6], Harlan E. Spence[7], and Donald G. Mitchell[3]

[1]Department of Atmospheric and Oceanic Sciences, UCLA, Los Angeles, CA, USA, [2]Center for Space Physics, Boston University, Boston, MA, USA, [3]Johns Hopkins University Applied Physics Laboratory, Laurel, MD, USA, [4]Space Science and Applications Group, Los Alamos National Laboratory, Los Alamos, NM, USA, [5]Space Sciences Division, New Mexico Consortium, Los Alamos, NM, USA, [6]Center for Solar-Terrestrial Research at New Jersey Institute of Technology, Newark, NJ, USA, [7]Institute for the Study of Earth, Oceans, and Space, University of New Hampshire, Durham, NH, USA

Abstract The composition of the inner magnetosphere is of great importance for determining the plasma pressure and thus the currents and magnetic field configuration. In this study, we perform a statistical survey of equatorial plasma pressure distributions and investigate the relative contributions of ions and electron with different energies inside of geostationary orbit under two auroral electrojet levels based on over 60 months of observations from the Helium, Oxygen, Proton, and Electron and Radiation Belt Storm Probes Ion Composition Experiment mass spectrometers onboard Van Allen Probes. We find that the total and partial pressures of different species increase significantly at high auroral electrojet levels with hydrogen pressure being dominant in the plasmasphere. The pressures of the heavy ions and electrons increase outside the plasmapause and develop a strong dawn-dusk asymmetry with ion pressures peaking at dusk and electron pressure peaking at dawn. In addition, ring current hydrogen with energies ranging from 50 keV up to several hundred keV is the dominant component of plasma pressure during both quiet (>90%) and active times (>60%), while oxygen with $10 < E < 50$ keV and electrons with $0.1 < E < 40$ keV become important during active times contributing more than 25% and 20% on the nightside, respectively, while the helium contribution is generally small. The results presented in this study provide a global picture of the equatorial plasma pressure distributions and the associated contributions from different species with different energy ranges, which advance our knowledge of wave generation and provide models with a systematic baseline of plasma composition.

Key Points:
- We performed a statistical survey of plasma pressure and the relative contributions from ions and electrons with different energies
- H^+ of hundreds of keV is the main contributor of plasma pressure that dominates inside plasmapause during geomagnetically quiet time
- The energy flux of H^+ with $0.1 < E < 40$ keV and O+ with $10 < E < 50$ keV increase significantly on the nightside during high AE intervals

Supporting Information:
- Figure S1

Correspondence to:
C. Yue,
yuechao@atmos.ucla.edu

Citation:
Yue, C., Bortnik, J., Li, W., Ma, Q., Gkioulidou, M., Reeves, G. D., et al. (2018). The composition of plasma inside geostationary orbit based on Van Allen Probes observations. *Journal of Geophysical Research: Space Physics*, *123*. https://doi.org/10.1029/2018JA025344

Received 13 FEB 2018
Accepted 14 JUL 2018
Accepted article online 24 JUL 2018

1. Introduction

Plasma pressure is a macroscopic parameter that plays an important role in plasma dynamics and generation of electric currents. Increasing plasma pressure gradients in the radial direction causes stretching of magnetic field lines and enhances perpendicular currents flowing azimuthally. On the other hand, the azimuthal plasma pressure gradient generates field-aligned currents, resulting in bending of magnetic field lines. There are many previous reports addressing the plasma pressure distributions in the inner magnetosphere. For example, Spence et al. (1989) constructed empirical radial profiles of the plasma pressure from the midtail to the inner magnetosphere by combining International Sun-Earth Explorer-2 with Active Magnetospheric Particle Tracer Explorers/Charge Composition Explorer measurements as a function of magnetic activity. Daglis et al. (1993) and Lui (2003) used Active Magnetospheric Particle Tracer Explorers/Charge Composition Explorer measurements to construct the equatorial plasma pressure distribution under different geomagnetic disturbance levels. Both Spence et al. (1987) and Lui et al. (1994) used empirical magnetic field models along with magnetohydrostatic equilibrium principles to infer how plasma pressure and pressure anisotropy evolves radially from the magnetotail inward to the heart of the ring current. Most recently, Wang et al. (2011) used Time History of Events and Macroscale Interactions during Substorms and Geotail data to investigate statistically the distributions of ions and electrons from the midtail to the inner magnetosphere and compared them with results from the rice convection model. Wang et al. (2013) and Yue et al. (2015) extended the above work by developing empirical plasma pressure models based on statistical observations of ion and electron fluxes in the equatorial region from Time History of Events and Macroscale Interactions during Substorms and

Geotail. C:son Brandt et al. (2002) utilized energetic neutral atom emissions at low altitude to infer the evolution of the global plasma pressure distribution during storms and substorms. With low-altitude measurements from the DMSP satellite and T89 magnetic field model, Wing and Newell (2002) obtained the two-dimensional plasma pressure distribution near the equator, operationalizing the modeling approach described earlier by Hirsch et al. (1996) for such use of low-altitude pressure measurements.

The ring current pressure is made up mainly of the hydrogen (H^+), oxygen (O^+), and helium (He^+) ions and electrons. Systematic dynamic changes in the spatial structure of ring current ions and electrons in the inner magnetosphere are essential to understand the ring current pressure variation. It is well known that, while the ion pressure in the inner magnetosphere is dominated by H^+ during quiet times, O^+ ions make a nonnegligible and sometimes dominant contribution to the ion pressure and the strength of the ring current. In situ observations and modeling work (e.g., Claudepierre et al., 2016; Daglis et al., 1999; Denton et al., 2005; Ebihara et al., 2006; Fok et al., 2001; Kistler et al., 2016; Lui, 2003; Yue et al., 2011) have confirmed that singly charged O^+ ions that originate in the Earth's ionosphere make a significant contribution to the plasma pressure in the Earth's inner magnetosphere during active times. There are numerous studies addressing the plasma composition changes as a function of geomagnetic disturbances, but most studies have focused on geostationary orbit or beyond (e.g., Forster et al., 2013; Fu et al., 2001; Kistler & Mouikis, 2016; Liu et al., 2005; Maggiolo & Kistler, 2014) due to a lack of in situ measurements of different species with sufficiently wide energy coverage and/or satellite orbital coverage at lower L shells (e.g., Keika et al., 2013). However, due to the observations of the recently launched Van Allen Probes, we are now able to provide a global view of the spatial distribution of the ring current inside of geosynchronous orbit and the relative contributions from different species. The Van Allen Probes mission is designed for operation in the radiation belts and provides a comprehensive picture of the in situ equatorial plasma composition from ~eV to ~MeV energies without significant background radiation contamination.

There are some case and statistical studies that have investigated the ion composition using Van Allen Probes under different geomagnetic activities. For example, Zhao et al. (2015) investigated the evolution of ring current ion energy density and energy content during geomagnetic storms and concluded that ions with energies $E < 50$ keV contribute more significantly to the ring current than those with higher energies during the storm main phase, while the higher energy protons dominate during the recovery phase and quiet times. Jahn et al. (2017) studied the relative abundances and absolute densities of warm plasma (>30 eV) measured by Helium, Oxygen, Proton, and Electron (HOPE) mass spectrometers onboard Van Allen Probes and found that warm O^+ is the most abundant close to the plasmapause, whereas warm H^+ dominates at higher L shells. Denton et al. (2017) performed a survey of 54 calm-to-storm events and 21 active-to-calm events to investigate the ion composition changes using the HOPE instrument and found that H^+ is the dominant ion in the plasma sheet in the calm-to-storm transition while heavy ions (O^+ and He^+) become increasingly important during extended calm intervals as charge exchange reactions result in a faster loss of H^+ than either O^+ or He^+. Fernandes et al. (2017) performed a statistical study to examine the abundances of 0.1–30 keV O^+ flux relative to H^+ flux as a function of Kp, L shell, magnetic local time (MLT), and energy by using the HOPE instrument and found that at $L = 6$ the O^+/H^+ ratio increases with increasing Kp, whereas at $L < 5$ the O^+/H^+ ratio generally decreases with increasing Kp.

While previous studies based on Van Allen Probes observations have presented important features of the ion composition changes driven by different geomagnetic disturbances, their studies are either only focused on one particular plasma population such as the warm plasma cloak or the plasma sheet or ring current particles (e.g., Denton et al., 2017; Jahn et al., 2017), or limited to a case study at particular MLT (e.g., Zhao et al., 2015). As shown from our previous study by Yue, Bortnik, Chen, et al. (2017), different populations behave differently. In order to provide a comprehensive view of the spatial distribution of plasma pressure inside of geostationary orbit and the relative contributions of various species with different energies under different AE levels, we perform a statistical study by using data from the HOPE and Radiation Belt Storm Probes Ion Composition Experiment (RBSPICE) instruments onboard both Van Allen Probes. Combining data from these two instruments, we are able to investigate the energy dependent contributions of ions from 1 eV to ~1 MeV and electrons from 15 eV to 1 MeV to the plasma pressure inside of geosynchronous orbit.

This paper is organized as follows. In section 2, we briefly describe the particle measurements used in this study and the methodology of our statistical analysis. The detailed statistical results are presented in

section 3. In section 4, we discuss the role of ions and electrons with different energy ranges contributing to the plasma pressure. Section 5 summarizes our results and outlines the main conclusions.

2. Data Set and Methodology

The Van Allen Probes (RBSP) mission, which consists of two identically instrumented spacecraft (probes A and B), was launched into near-equatorial orbit (10° inclination) on 30 August 2012. They have an orbital period of ~9 hr, a perigee at ~1.1 R_E, and an apogee at ~5.8 R_E (Mauk et al., 2013). Both satellites are equipped with comprehensive suites of particles and field measurement instrumentation. Here we perform our statistical analysis by using the level-3 omnidirectional and unidirectional differential flux measurements from the HOPE mass spectrometer (Funsten et al., 2013) of the Energetic Particle Composition and Thermal Plasma Suite (Spence et al., 2013) and the RBSPICE (Mitchell et al., 2013) instrument onboard Van Allen Probes (both A and B) from October 2012 to December 2017, during which the apogees of the satellites covered all MLT sectors more than twice near the equator. The combined measurements from both instruments cover the H^+ energy from ~1 eV to 600 keV with 85 energy channels (HOPE: 1 eV–44 keV of 71 channels and RBSPICE: 45–600 keV of 14 channels), O^+ energy from ~1 eV to ~1 MeV with 81 channels (HOPE: 1 eV–52 keV of 72 channels and RBSPICE: 142 keV–1.1 MeV of 9 channels), He^+ energy from ~1 eV to ~500 keV with 81 channels (HOPE: 1 eV–52 keV of 72 channels and RBSPICE: 65–520 keV of 9 channels), and electron (e^-) energy from 15 eV to ~1 MeV with 127 energy channels (HOPE: 15 eV–18 keV of 63 energy channels and RBSPICE: 20–940 keV of 64 energy channels). It should be noted that there is no charge state separation for both HOPE and RBSPICE instruments. Here we assume that all the measurements are single charged particles. HOPE data have 11 pitch angle (PA) bins ranging from 0° to 180° with 18° width, except for the first and last PA bins that are 9° wide. Meanwhile, the level 3 RBSPICE data are binned into 17 PA bins with 10° width, but 15° width for the first and last PA bins. The observed flux of each energy channel from the HOPE instrument has been corrected according to the instantaneous spacecraft potential as done in our previous studies (e.g., Yue, An, et al., 2016; Yue, Bortnik, Chen, et al., 2017; Yue, Bortnik, Thorne, et al., 2017; Yue, Chen, Bortnik, et al., 2017; Yue, Li, et al., 2016). In addition, we obtain the total electron number density preferentially from high-frequency receiver spectra of the Electric and Magnetic Field Instrument Suite and Integrated Science instrument (Kletzing et al., 2013). If it is not available, the electron number density is obtained from the spacecraft potential measured by the electric field and waves instrument (Wygant et al., 2013).

Here we use the unidirectional fluxes to calculate the plasma pressure of four different species in the parallel and perpendicular directions as well as the total plasma pressure as follows:

Considering relativistic effects, the particle phase space density (PSD) is calculated as $PSD = \frac{\gamma^3 m_0 f}{v^2}$, where γ is the relativistic factor, f is the differential energy flux, m_0 is the particle's rest mass, and v is the velocity. The γ and v are calculated using the relations

$$E = (\gamma - 1)m_0c^2 \text{ and} \frac{v^2}{C^2} = 1 - \frac{1}{\left(\frac{E}{m_0c^2} + 1\right)^2}$$

where c is the speed of light and E is the particle's kinetic energy. By using the PSD, the perpendicular and parallel plasma pressure $P_\perp$ and $P_\parallel$ of each species are then calculated as (De Michelis et al., 1999; Siscoe, 1983)

$$P_\perp = \int_{v_{min}}^{v_{max}} \int_0^\pi \pi \sin^3(\alpha) m_0 v^4 PSD d\ \alpha dv$$

$$P_\parallel = \int_{v_{min}}^{v_{max}} \int_0^\pi 2\pi \sin(\alpha) \cos^2(\alpha) m_0 v^4 PSD d\ \alpha dv$$

where α is the PA. The integral in particle velocity was performed over the entire electron and ion energy ranges from HOPE and RBSPICE, and v_{min} and v_{max} are the minimum and maximum velocities corresponding to the energy range of the instrument. The partial plasma pressure of different species is $P = \frac{2P_\perp + P_\parallel}{3}$, and the total plasma pressure is the sum of partial plasma pressures from different species including H^+, O^+, and He^+ and electrons.

In order to investigate how particle injections affect the plasma pressure distributions near the equator, we binned data into MLT and radial distance according to two different AE levels: AE $<$ 100 nT for quiet times (e.g., Hsu & McPherron, 2012; Yue et al., 2010) and AE $>$ 300 nT for active times (e.g., Meredith et al., 2003). These criteria were chosen to include sufficient data for statistically significant results and to provide a clear separation of the two distinct geomagnetic conditions. In addition, we have constrained our observational database to periods when the Van Allen Probes were near the equator with magnetic latitudes |MLAT| $<$ 5° in order to obtain the equatorial plasma pressure distributions, and all data were averaged into 1-min time resolution. We selected data points when both HOPE and RBSPICE data were available without limiting the *L* shell value. It should be noted that the median value was used for our statistical results throughout the paper since the distribution would not be fully characterized with the mean and the standard deviation alone if the distribution is not a normal one.

3. Results

Comprehensive ion measurements from Van Allen Probes enable us to analyze the details of the plasma composition and corresponding contributions to the plasma pressure inside of geostationary orbit. In this section, we first show one case study on 26 to 28 August 2014 to illustrate how the pressure and energy spectra of different species vary as geomagnetic activity changes. Statistical results of plasma pressure distributions and energy spectra of different species then follow.

3.1. Case Study

Figure 1 illustrates the plasma pressure as the magnetosphere changes from quiet to active conditions, occurring on 27 August 2014 and observed by Van Allen Probe B with an apogee near the dawn sector (Figure 1a). As shown in Figures 1b–1d, the magnetosphere is relatively quiet before 3 UT on 27 August (red dashed vertical line). Following the strong southward turning of the interplanetary magnetic field (Figure 1b), there is a typical coronal mass ejection driven storm occurring with a minimum sym-H of −90 nT around 16:30 UT on 27 August (Figure 1d). Meanwhile, there is substorm activity with several AE peaks around 1,200 nT (Figure 1c) occurring near the time of minimum sym-H (Figure 1d). Figure 1e shows the ion and electron pressures and total plasma pressure indicated by different colors with total plasma pressure in black, H^+ pressure in blue, O^+ pressure in red, He^+ pressure in cyan, and electron pressure in green. During quiet time (the first three full orbits of Van Allen Probe B), the H^+ pressure is the dominant contributor to the plasma pressure. After the onset of geomagnetic activity (the vertical dashed line), especially during high AE interval and storm main phase, the pressures of the different species increase dramatically and O^+ pressure becomes comparable to the H^+ pressure.

In order to elucidate which energy range is the dominant contributor from the four different species to the pressure increase, we plot the omnidirectional energy fluxes of electrons, H^+, He^+, and O^+ as a function of energy in Figures 1f–1i, respectively. The large missing data points within $E < 5$ eV shown in ion energy spectra in Figures 1g–1i are due to the spacecraft potential effect that we have corrected. It should be noted that the discrepancy of flux level around 20 keV of electrons and 50 keV of ions is due to the difference in flux level between HOPE and RBSPICE. During the quiet time, there is a persistent ring current composed of H^+ ions, with energies ranging from ~50 keV to several hundred keV (depending on *L* shell), which is the dominant component to the quiet time plasma pressure. As geomagnetic activity increases, there are clear substorm injections at high *L* shells outside the plasmasphere and energy fluxes of electrons, H^+, and O^+ with energies of several hundred eV to tens of keV showing dramatic increases.

3.2. Statistical Results

The case shown in Figure 1 is an example of the plasma composition change that occurs in the dawn sector. In order to understand the systematic distribution of the plasma pressure and its dependence on different species with energies from different populations at various MLT and *L* shells under different geomagnetic conditions, we perform a comprehensive statistical survey based on more than 5 years of Van Allen Probes observations. Here we separate our database by different AE intervals to examine how substorm injections affect the ring current pressure distribution on the equatorial plane inside of geostationary orbit.

Figure 2 shows the statistical distributions of the median values of plasma pressure and the relative contributions from different species on the equatorial plane separated into two AE ranges: AE $<$ 100 nT (columns a

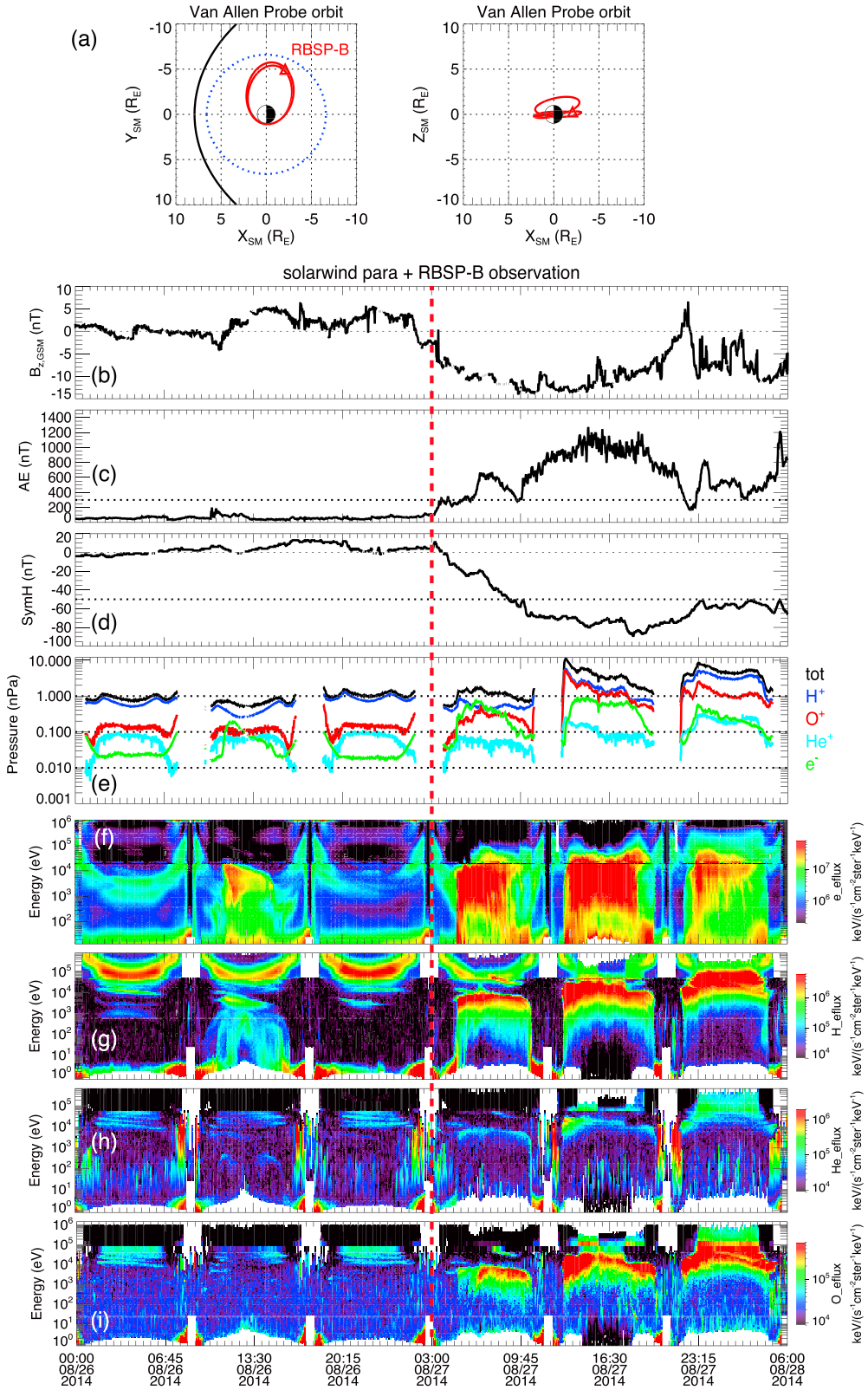

Figure 1. The plasma pressure variation observed by Van Allen Probe B from 26 to 28 August 2014. (a) Van Allen Probe B orbit projection on solar magnetic *X-Y* and *X-Z* planes; (b) interplanetary magnetic field B_z component; (c) auroral electrojet index; (d) sym-H index; (e) ions and electron plasma pressures and total plasma pressure with dark blue for H^+, red for O^+, cyan for He^+, green for electron, and black for the total plasma pressure; (f–i) the energy spectrograms of energy flux for electrons, H^+, He^+, and O^+ ions, respectively.

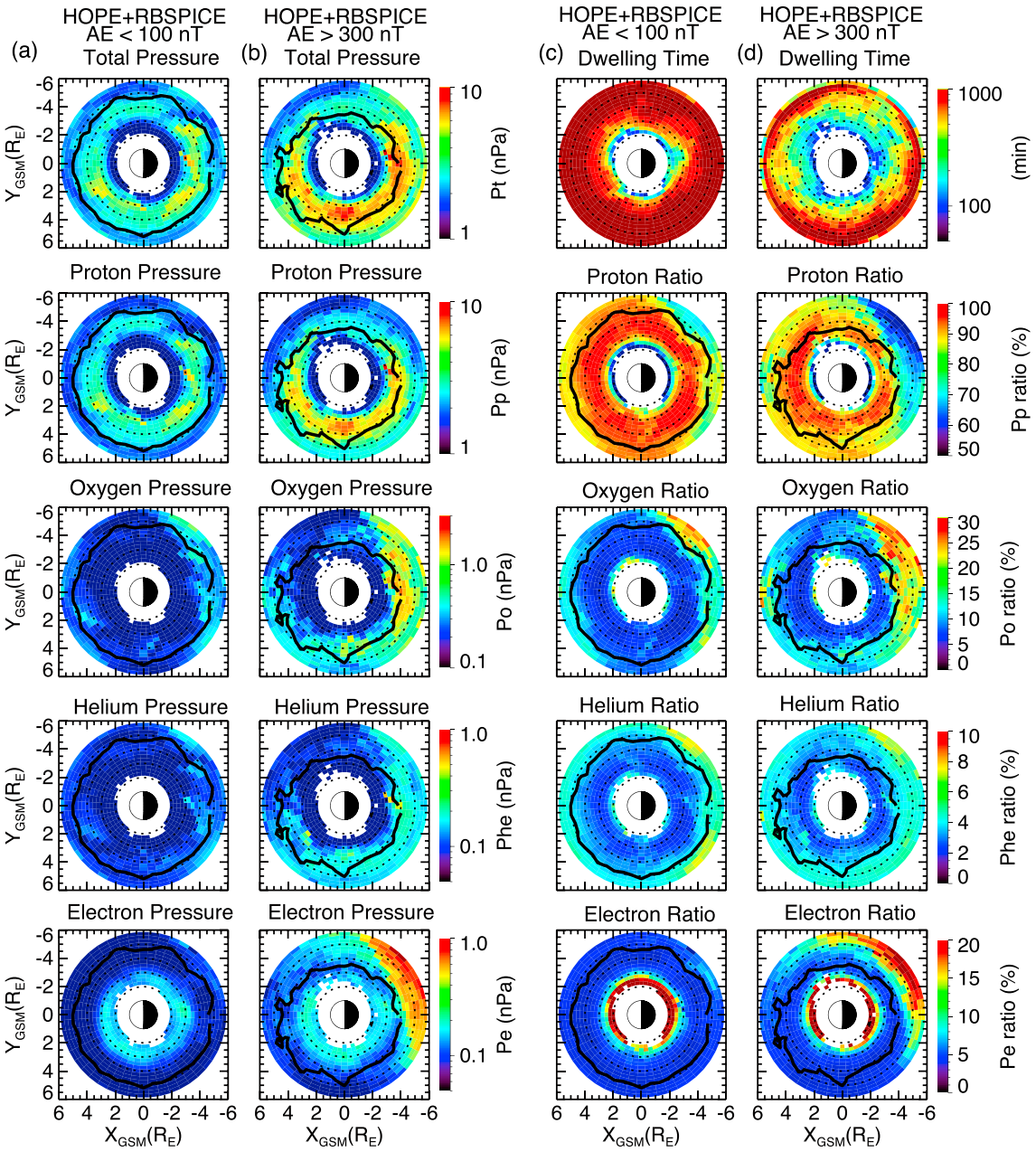

Figure 2. The statistical distributions of median plasma pressure on the equatorial plane under two auroral electrojet (AE) levels: AE $<$ 100 nT and AE $>$ 300 nT. (a and b) The panels from top to bottom are total plasma pressure; H^+, O^+, and He^+ ions; and electron pressures; (c and d) the panels from top to bottom are the satellite dwell time; H^+, O^+, and He^+; and electron pressure ratios which are the ratios between the partial plasma pressure of the different species and the total plasma pressure. The overplotted black lines are the plasmapause locations defined as when the median value of electron number density is at 80 cm^{-3}.

and c) and AE $>$ 300 nT (columns b and d). The overplotted black lines are the plasmapause locations defined as the point where the median value of electron number density is at 80 cm^{-3}. The top panels of Figure 2c and 2d show the satellite dwell time during these two conditions. Though the data number is smaller during active times compared with that during quiet times, the absolute values (>100) are still large enough to represent statistically significant results (the typical range of pressure variations is presented in the supporting information to demonstrate the significance of our statistical results). The panels from top to bottom depict total plasma pressure, followed by H^+, O^+, and He^+ and electron pressures in Figures 2a and 2b. It is shown that the total plasma pressure is more or less symmetric at all MLT and peaks around L = 4 inside the plasmasphere during quiet times (Figure 2a), while the total plasma pressure shows a strong

dawn-dusk asymmetry with pressure peaks around the dusk side during active times (Figure 2b). In addition, the plasmasphere erodes and H^+, O^+, and He^+ and electron pressures all increase during periods of high AE levels on the nightside with H^+ pressure dominating inside the plasmasphere and heavy ions and electron pressures increasing outside the plasmapause. This could be due to the fact that during high AE interval, the plasmapause location is only modestly impacted, while the ions could penetrate fairly deep into the inner magnetosphere to lower *L* shells and result in the observed stronger partial pressures. A strong dawn-dusk asymmetry is also observed with ion pressures peaking from dusk to postmidnight (consistent with drift physics theoretical models described in a series of papers by Kivelson & Spence, 1988 and Spence & Kivelson, 1990, 1993 and also with the related results of Keesee et al., 2011 based on TWINS energetic neutral atom observations) while electron pressure peaking around the premidnight to dawn side. This dawn-dusk asymmetry of ion pressure has also been reported by Kronberg et al. (2015), in which the spatial distributions of energetic protons and O^+ (>274 keV) are established based on 7 years Cluster observations. Regarding the relative contribution to the total plasma pressure as shown in Figures 2c and 2d (the panels from top to bottom are the dwell time, H^+, O^+, and He^+, and electron pressure ratios which are the ratios between partial plasma pressure of different species and total plasma pressure), H^+ is the dominant contributor to the total plasma pressure during both quiet (>90% inside the plasmasphere and >70% outside) and active (>80% inside plasmasphere and >60% outside) times with a larger contribution on the dayside than that on the nightside in general due to smaller contributions from other species on the dayside. Meanwhile, the contributions from O^+ ions and electrons also increase from ~10% and ~5% to 25% and 20%, respectively, at high *L* shells outside the plasmasphere on the night side, while the contribution from He^+ ions has almost no change by comparing the active and quiet time states.

In order to investigate more specifically what energy ranges of different species contribute to the pressure increase and where the biggest changes are located, we plot the omnidirectional energy flux of each species under two AE levels (AE < 100 nT and AE > 300 nT) and the flux ratio between these two conditions in Figures 3 to 6. Figure 3a shows the H^+ energy flux spectrum from 1 eV to 600 keV as a function of *L* shell on the abscissa. The left and right columns represent two different AE levels, and panels from top to bottom represent different MLT sectors as indicated by the label above each panel. As shown, there is a persistent MLT-symmetric ring current composed of H^+ ions of hundreds of keV depending on *L* shell, which is the main contributor to the symmetric ring current pressure during both quiet and active times. In addition, there are plasma sheet particles with energies from 1 to 20 keV on the nightside at large *L* shells ($L > 4.5$) during quiet times, while the flux becomes much more intense and extends to lower energies of 0.5 keV and smaller *L* shells as AE increases with ~10-keV particles moving deeper toward the Earth due to the competition of electric and magnetic drifts.

Furthermore, the warm plasma cloak population with energies ranging from ~10 to ~500 eV becomes prominent from the premidnight to the dawn sector around $3.5 < L < 5$ during active times. Yue, Bortnik, Thorne, et al. (2017) found that these warm plasma cloak H^+ ions are field-aligned, indicating that these H^+ ions probably originate from the midlatitude ionosphere. Figure 3b shows the flux ratio between AE > 300 nT and AE < 100 nT as a function of energy and *L* shell at different MLTs to (1) better demonstrate the relative contributions of various populations at different locations and (2) minimize the difference between HOPE and RBSPICE flux level measurements as shown in energy spectrum plots in Figure 1 and Figures 3a–6a. The overplotted solid and dashed lines in each panel depict the constant flux ratio of 0.5 and 5 so as to highlight the regions with the most flux reductions and enhancements from quiet time to active time, respectively. It is shown that both the high-energy portion (10 keV < *E* < 40 keV) and low-energy portion (10 eV < *E* < 10 keV) of H^+ energy fluxes increase and peak around $3.5 < L < 5$ near the midnight (21–03 MLT) region. Away from the midnight region, the *E* < 10 keV portion increases dramatically on the dawn side and *E* > 10 keV portion increases on the dusk side. This is caused by the different drift paths of particles with *E* > ~10 keV H^+ drifting toward dusk due to the dominant magnetic gradient and curvature drifts while *E* < 10 keV H^+ drifting toward the dawn side due to the dominant corotational electric drift.

In contrast to the H^+ ions, as shown in Figures 4 and 5, the energy flux of the heavy ions (O^+ and He^+) peaks around 10 to 100 keV, which is the main energy range contributing to the total plasma pressure. As AE increases, the flux of these high-energy (*E* > 10 keV) heavy ions, especially O^+, shows a dramatic increase on the nightside and injections extending deeper (*L* = ~3.5) toward the Earth for 10-keV particles around

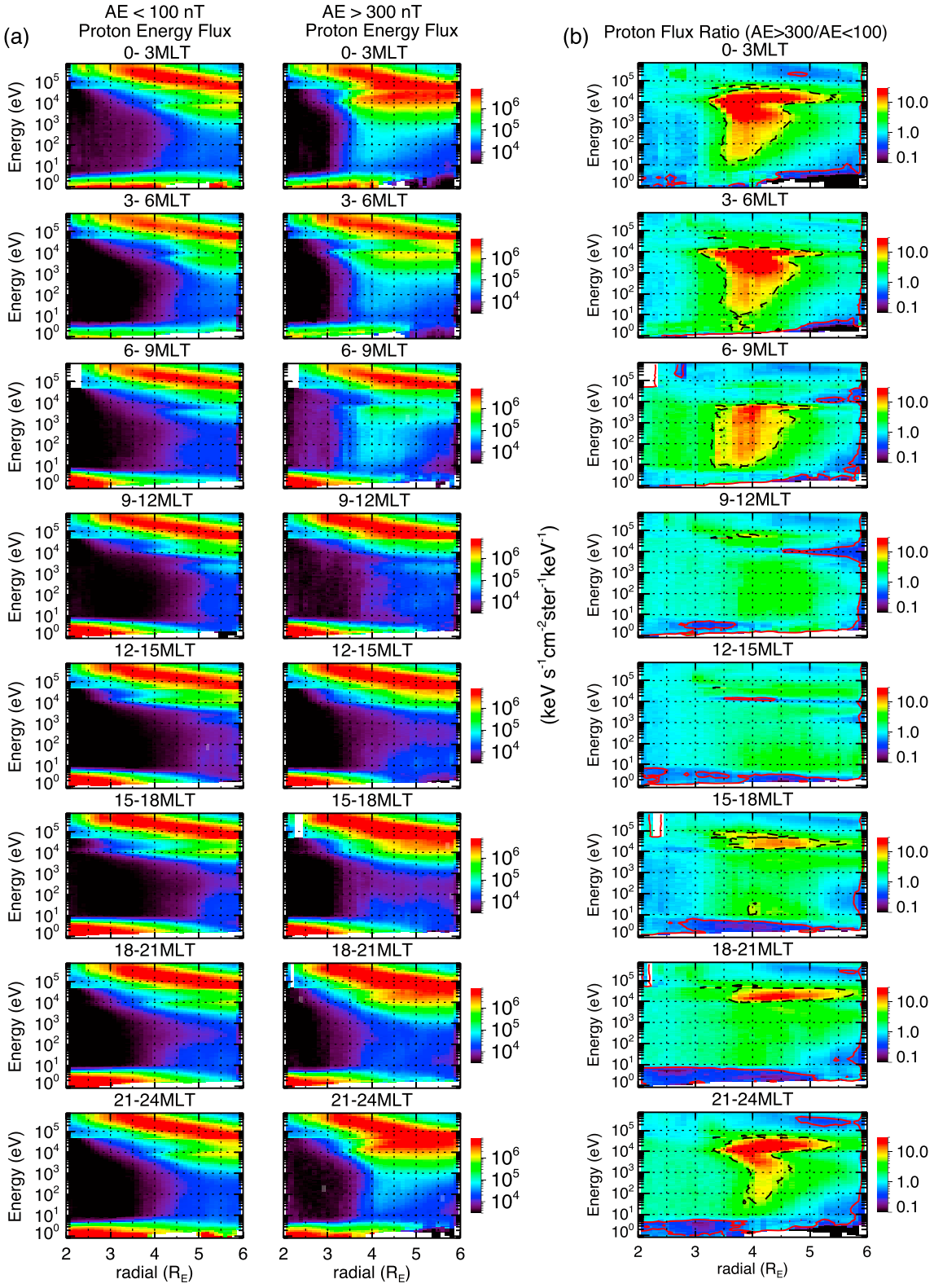

Figure 3. (a) The statistical distributions of median H^+ energy flux as functions of energy and *L* shell on the equatorial plane under two auroral electrojet (AE) levels: AE $<$ 100 nT and AE $>$ 300 nT. (b) The H+ flux ratio between those with AE $>$ 300 nT and AE $<$ 100 nT as functions of energy and *L* shell on the equatorial plane. The panels from top to bottom for each column are for different magnetic local time sectors as indicated by the label on top of each panel. The overplotted solid red and dashed black lines in each panel are the constant flux ratio of 0.5 and 5 to highlight the most flux reductions and enhancements from quiet time to active time, respectively.

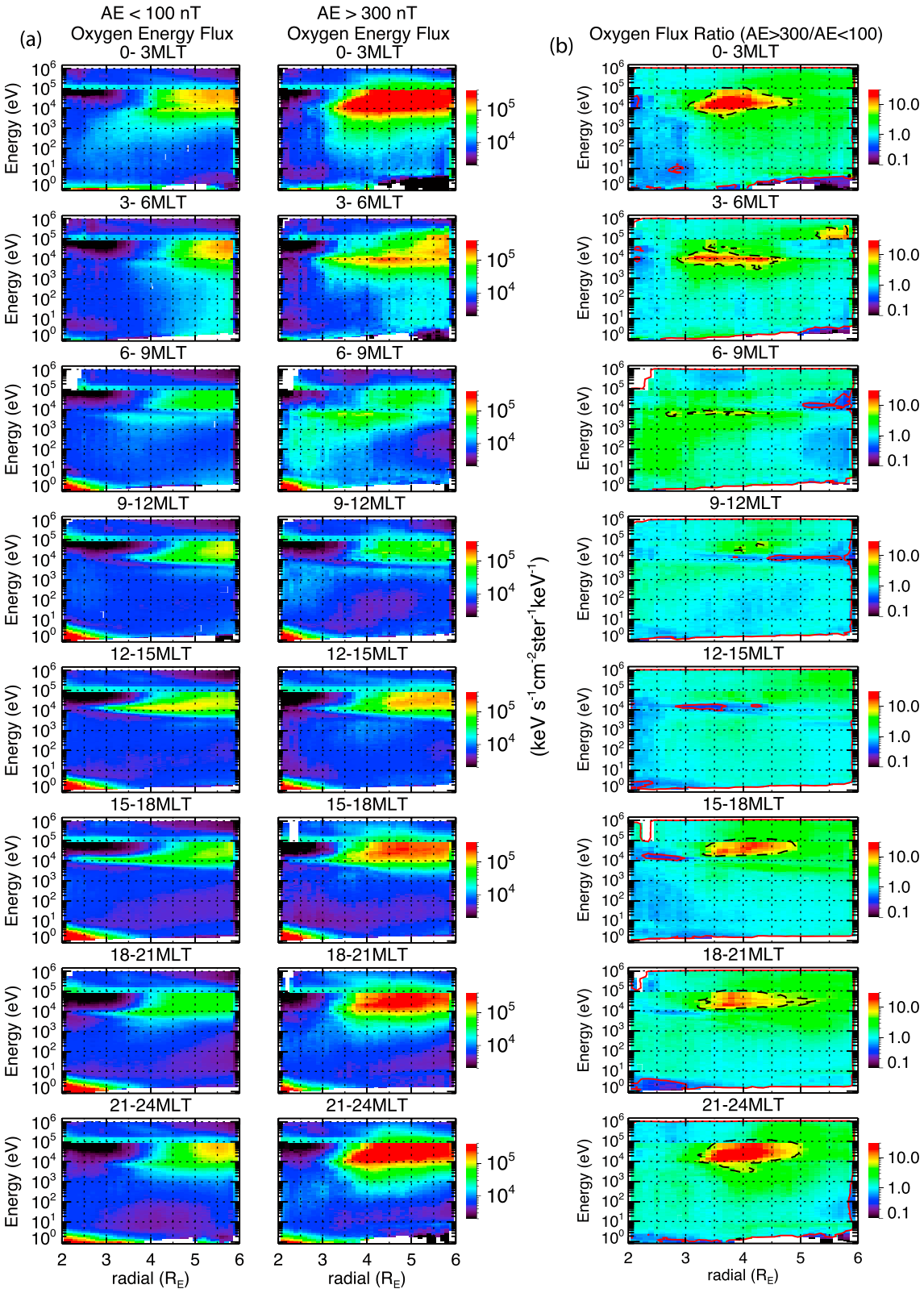

Figure 4. The energy flux and flux ratio of O^+ with the same format as in Figure 3.

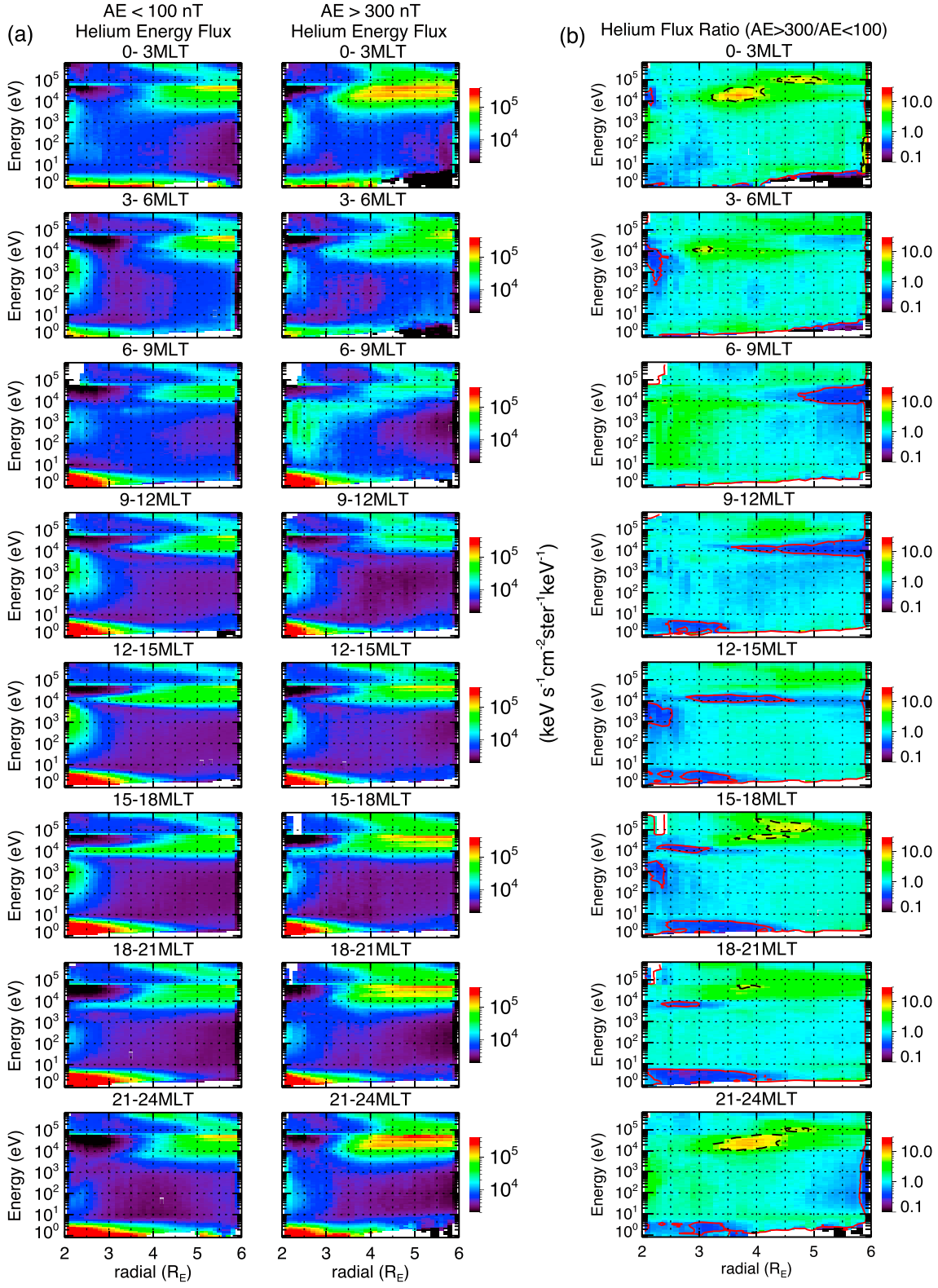

Figure 5. The energy flux and flux ratio of He^+ with the same format as in Figure 3.

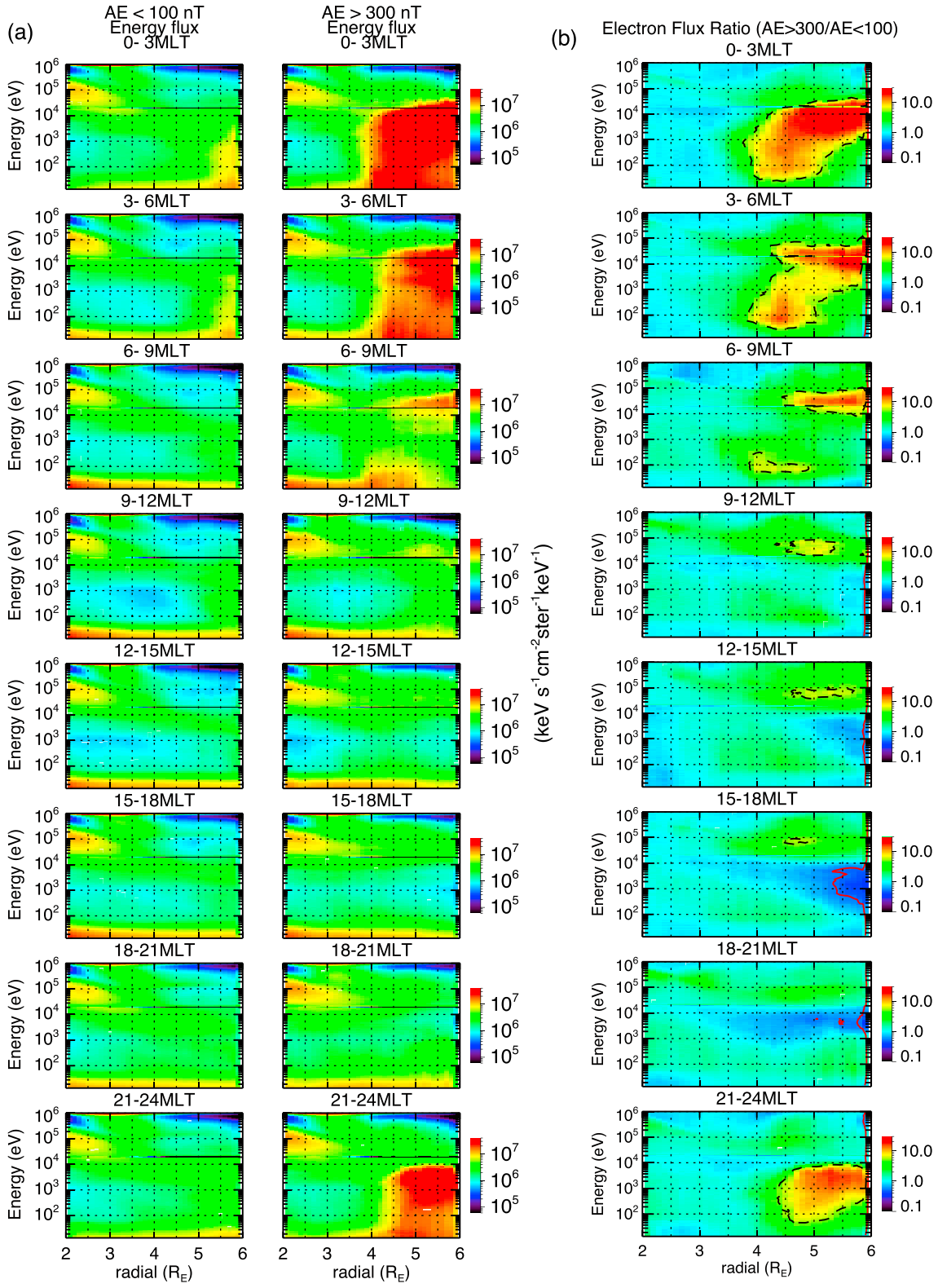

Figure 6. The energy flux and flux ratio of electrons with the same format as in Figure 3.

post midnight. These injected tens of keV O^+ drift from the midnight sector toward duskside (Figure 4b) and form high O^+ plasma pressures as shown in Figure 2b. Compared to the O^+ flux ratio during active and quiet time (Figure 4b), the He^+ flux ratio (Figure 5b) is much smaller, indicating that the He^+ flux has a weaker dependence on geomagnetic activity. The substantially larger increases of O^+ compared to the He^+ during active time are probably related to their different origins where majority of He^+ (no charge separation in HOPE and RBSPICE instruments, so we do not differentiate He^+ or He^{++} in this study) in the magnetosphere is of solar wind origin while O^+ is ionospheric origin. During active time, the ionospheric outflow is enhanced while the He^+ of solar wind origin changes insignificantly (Sharp et al., 1982). It should be noted that the O^+ energy spectrum plot presented here has an energy gap over ~50–140 keV. In order to determine the dominant energy range contributing to the O^+ pressure increase, we have added the RBSPICE TOFxPH data with energies from 50 to 140 keV in Figure S10 in the supporting information, even though the measurements from TOFxPH are contaminated (as shown in Figure S10a that the flux is larger for energies from 50 to 140 keV compared to those of energies below and above, especially at $L < 4$). It is shown in S10b that the O^+ flux ratio peaks around energies from 10 to 50 keV on the nightside, and the contribution from 50–140 keV is relatively small, which in turn confirms that O^+ pressure is unlikely to be affected significantly by this energy gap (Figures S8 and S9 show the difference of O^+ pressure without and with TOFxPH data, and the O^+ pressure is quite similar at $L > 4$, and O^+ pressure is overestimated at $L < 4$ when it includes TOFxPH data).

Figure 6 shows the electron energy spectrum in the same format as Figure 3. It is shown in Figure 6a that there is strong injection of electron fluxes from the tail plasma sheet during high AE interval. The energy range is from 0.1 to 40 keV in the postmidnight and 0.1 to 8 keV at premidnight, and the postmidnight injection extends deeper compared with premidnight during high AE interval shown in Figure 6b. In addition, a strong depletion of electrons from 0.1 to 10 keV in the dusk sector is observed as shown in Figure 6b, which is probably due to chorus wave scattering loss when electrons drift through the dawn sector (e.g., Li et al., 2010; Tao et al., 2011) combined with the contraction of the Alfvén layer as AE increases, so that particles previously on closed drift paths are now on the open drift paths, implying that these particles cannot access the dusk sector.

4. Discussion

Knowledge of the ion composition in the near-Earth magnetosphere and plasma sheet is essential for the analysis of magnetospheric processes and related instabilities. In our statistical study focused on the region within geosynchronous orbit, we find that the total and H^+ plasma pressures usually dominate inside the plasmasphere and ion and electron partial pressures increase as geomagnetic activity increases while the H^+ is the dominant species contributing to the total plasma pressure during both quiet (90%) and active (60%) time. On the other hand, O^+ and electron contributions increase from less than 10% and 5% to more than 25% and 20% on the nightside at $L > 4$ outside the plasmapause. However, the He^+ contribution has almost no change. Similar results have been found during storm periods. For example, Greenspan and Hamilton (2002) statistically investigated H^+ and O^+ contributions to ring current energy during 67 geomagnetic storm cases from year 1985 to 1989 around solar minimum and showed that the O^+ energy density is lower than the H^+ energy density for 94% of the storm events and that the O^+ contributes to less than 23% of the ring current energy in most of the cases (72% of the storms). In this study, we have used Van Allen Probe data from October 2012 to December 2017 during which the solar activity is relatively weak, although year 2014 is around solar maximum (solar cycle 24 which started from year 2009 to 2018 is a relatively weak solar cycle). The low percentage of O^+ contribution to the plasma pressure might be related to this relatively quiet condition on the Sun that changes O^+ composition in the topside ionosphere.

The distributions of the equatorial partial plasma pressures provide insight into the potential for wave excitation. For instance, it is shown that electron pressure increases predominantly at the dawn sector outside the plasmapause during high AE level, which likely corresponds to the excitation region of chorus waves which, in turn, cause loss of plasma sheet electrons and the acceleration of radiation belt relativistic electrons (e.g., Baker et al., 2014; Horne et al., 2005; Li et al., 2007; Lorentzen et al., 2001; Ni et al., 2014; Reeves et al., 2013; Thorne, Li, Ni, Ma, Bortnik, Baker, et al., 2013; Thorne, Li, Ni, Ma, Bortnik, Chen, et al., 2013). In addition, the ring current H^+ pressure increases predominantly inside the plasmasphere on the dusk side during

geomagnetically active conditions, indicating that EMIC wave excitation probably occurs in the region of overlap of energetic ions and dense plasmaspheric plasma (e.g., Cornwall et al., 1970), which could lead to EMIC-driven precipitation.

Regarding the energy range that has the most significant contribution to the ring current pressure, Zhao et al. (2015) have investigated a moderate storm case in detail by using Van Allen Probes around the midnight region and found that ions with energies <50 keV contribute more significantly to the ring current than those with higher energies during the storm main phase and the higher energy protons dominate during the recovery phase and quiet times. In addition, the contribution from O^+ is ~25% of the ring current energy content during the main phase and the majority of that comes from <50 keV O^+. Since their study only separates the particle energies into two energy levels with low-energy range of $0.2 < E < 50$ keV and high-energy range of $50 < E < 1{,}000$ keV, respectively, it cannot resolve the contributions of plasma pressure from different energies in details. In this study, we have found that the persistent, MLT-symmetric ring current composed of H^+ ions of hundreds of keV (depending on L shell) is the main contribution to the plasma pressure inside geostationary orbit during quiet time, which is consistent with previous study done by Gkioulidou et al. (2016). As AE increases, the injection of H^+ from plasma sheet is from 0.1 to 40 keV, while the O^+ injection is dominant over $10 < E < 50$ keV (which is accelerated by adiabatic and nonadiabatic mechanisms in the plasma sheet) with 10-keV ions injected deeper toward the Earth. This energy range of ions forms the main contribution to the pressure increases during active time. The electron injection is from 50 eV to ~10 keV at premidnight, while the upper limit of injection at postmidnight is around 40 keV and further deep. These electrons are within the dominant energy range for the dramatic increase of electron pressure during active time in the dawn sector. Previous studies (e.g., Zhao et al., 2015) have discussed about possible HOPE instrument calibration issue, which could affect the calculated plasma pressure values during active time, since the pressure enhancement is mainly contributed by the plasma with energies <50 keV as shown in Figures 3 to 6. We have checked the results after including an increase in HOPE ion fluxes by a factor of 3 according to Zhao et al. (2015). As shown in Figure S12, the total pressure increases and the relative contributions from different species also change with electron contribution to the total plasma pressure becoming smaller (10%) and the O^+ pressure contribution increasing to more than 30% outside plasmapause on the nightside during active time compared with the results shown in Figure 2. The energy ranges of different species contributing to the plasma pressure increase and major conclusions, however, are unchanged.

Although we have observed net energy flux increase on the nightside during high AE levels, the loss process also becomes enhanced under geomagnetically active condition, and ions and electrons can be lost to the magnetopause depending on their drift paths. In addition, ions can be lost through Coulomb scattering (e.g., Ebihara et al., 1998), charge exchange (e.g., Tinsley, 1978), and precipitation, while electrons are mainly subjected to precipitation loss. The Coulomb collision and charge exchange losses are larger at lower L shells and most effective for particles that are more field-aligned (Fok et al., 1991). The ion precipitation loss is mainly due to the current sheet scattering depending on the magnetic field configuration (e.g., Sergeev et al., 1983; Yue et al., 2014) as well as wave-particle scattering (e.g., Liang et al., 2014). The electron precipitation loss is mainly due to wave-particle scattering (e.g., Abel & Thorne, 1998; Ni et al., 2014). As shown in Figures 3b to 6b indicated by the red solid lines, as AE increases, the ion flux around 10 keV decreases in the prenoon sector at high L shell, while a depletion of electrons from 0.1 to 10 keV is observed near the dusk sector at high L shell. These flux decreases are probably due to the strong loss process that intensifies as AE increases.

5. Summary and Conclusions

In this paper, we have performed a detailed statistical analysis of the equatorial plasma pressure distributions and the relative contributions from three ion species and electrons with different energies under two AE levels by using HOPE and RBSPICE measurements onboard both Van Allen Probes A and B from October 2012 to December 2017, in order to understand the characteristics of plasma composition under different geomagnetic conditions. Our main conclusions are as follows:

1. The ring current plasma pressure is maximized inside the plasmasphere during quiet time. The total and partial pressures of different species show significant increase at high AE levels on the nightside with H^+ pressure increasing inside the plasmasphere whereas heavy ions and electron pressure increasing outside

the plasmapause, creating a strong dawn-dusk asymmetry that is also observed with total and ion pressures larger toward dusk and electron pressure larger toward dawn.

2. Oxygen and electron contributions increase from less than 10% or 5% to more than 25% or 20% (these numbers would change if HOPE measurements are lower than real situations as we have discussed previously), while the H^+ ion contribution shows a significant decrease at post midnight to dawn at $L > 4$.
3. The persistent MLT-symmetric ring current, which is predominantly located inside the plasmasphere in a statistical sense, is composed of H^+ ions of hundreds of keV (depending on L shell) and is the main contributor to the plasma pressure during geomagnetically quiet (>90%) time.
4. As AE increases, the injection of H^+ ions from the plasma sheet is composed of energies extending from 0.1 to 40 keV, while the O^+ injection is dominated by $10 < E < 50$ keV, with ~10-keV ions injected deeper toward the Earth. These ions are the main contributors to the ion pressure increases during active time.
5. The electron injection is from 50 eV to ~10 keV at premidnight, while the upper limit of injection at postmidnight is around 40 keV and deeper to lower L shells ($L = 4$). These electrons are the dominant component for the dramatic increase of electron pressure near the dawn sector at active time.
6. There is a strong depletion of electrons from 0.1 to 10 keV in the dusk sector which is probably due to the combination of stronger loss of electrons through wave-particle interaction and shrinking of the Alfvén layer as AE increases, so that particles that were previously on closed drift paths now move on to open drift paths, and as a result, these particles cannot access the dusk sector.

Accurate knowledge of plasma pressure dependence on different species with different energy populations in the inner magnetosphere is important since it reflects the source, transport, and loss processes of electrons and ions of different populations. In this study, we have provided a general picture of the plasma composition and contributions to the plasma pressure as a function of MLT, L shell, and geomagnetic activity. To fully understand the dynamic process of plasma pressure inside the geosynchronous orbit, the time history should also be considered. As shown in Figure 1, the plasma pressure gradually builds up after geomagnetic activity increases and peaks around the early recovery phase, which is about 18 hr later from the storm sudden commencement. Simultaneously, the ion and electron energy range of peak energy fluxes also moves to higher energies during this interval. In order to track these changes, the universal time should be added as another dimension similar to the location, which is left for our future study of the plasma pressure investigation.

Acknowledgments

This work was supported by NASA LWS grant NNX14AN85G and NASA HTIDeS NNX16AG21G. Wen Li would like to acknowledge NASA grants NNX15AI96G and NNX17AG07G. Gkioulidou was supported by JHU/APL subcontract 131803 to the New Jersey Institute of Technology under NASA Prime contract NNN06AA01C. We acknowledge use of Van Allen Probes data of the Level 3 HOPE omni- and unidimensional particle flux data obtained from the RBSP-ECT website (rbsp-ect.lanl.gov/data_pub/rbspb/hope/level3/PA/), made publicly available through NASA prime contract number NAS5-01072; the Level 3 omni- and uni-dimensional RBSPICE particle flux data obtained from the RBSPICE website (http://rbspicea.ftecs.com/Level_3PAP/); and the level 3 high-frequency receiver data obtained from the RBSP Electric and Magnetic Field Instrument Suite and Integrated Science website (emfisis.physics.uiowa.edu/Flight/RBSP-B/L3). We thank the Space Physics Data Facility at the NASA Goddard Space Flight Center for providing the OMNI data (ftp://spdf.gsfc.nasa.gov/pub/data/omni/omni_cdaweb/).

References

Abel, B., & Thorne, R. M. (1998). Electron scattering loss in Earth's inner magnetosphere: 1. Dominant physical processes. *Journal of Geophysical Research*, *103*(A2), 2385–2396. https://doi.org/10.1029/97JA02919

Baker, D. N., Jaynes, A. N., Hoxie, V. C., Thorne, R. M., Foster, J. C., Li, X., et al. (2014). An impenetrable barrier to ultrarelativistic electrons in the Van Allen radiation belts. *Nature*, *515*(7528), 531–534. https://doi.org/10.1038/nature13956

Claudepierre, S. G., Chen, M. W., Roeder, J. L., & Fennell, J. F. (2016). An empirical model of ion plasma in the inner magnetosphere derived from CRRES/MICS measurements. *Journal of Geophysical Research: Space Physics*, *121*, 11,780–11,797. https://doi.org/10.1002/2016JA023468

Cornwall, J. M., Coroniti, F. V., & Thorne, R. M. (1970). Turbulent loss of ring current protons. *Journal of Geophysical Research*, *75*(25), 4699–4709. https://doi.org/10.1029/JA075i025p04699

Daglis, I. A., Sarris, E. T., & Wilken, B. (1993). AMPTE/CCE observations of the ion population at geosynchronous altitudes. *Annales de Geophysique*, *11*, 685–696.

Daglis, I. A., Thorne, R. M., Baumjohann, W., & Orsini, S. (1999). The terrestrial ring current: Origin, formation, and decay. *Reviews of Geophysics*, *37*(4), 407–438. https://doi.org/10.1029/1999RG900009

De Michelis, P., Daglis, I. A., & Consolini, G. (1999). An average image of proton plasma pressure and of current systems in the equatorial plane derived from AMPTE/CCE-CHEM measurements. *Journal of Geophysical Research*, *104*(A12), 28,615–28,624. https://doi.org/10.1029/1999JA900310

Denton, M. H., Thomsen, M. F., Korth, H., Lynch, S., Zhang, J. C., & Liemohn, M. W. (2005). Bulk plasma properties at geosynchronous orbit. *Journal of Geophysical Research*, *110*, A07223. https://doi.org/10.1029/2004JA010861

Denton, M. H. M. F., Thomsen, G. D., Reeves, B. A. L., Henderson, M. G., Jordanova, V. K., Fernandes, P. A., et al. (2017). The evolution of the plasma sheet ion composition: Storms and recoveries. *Journal of Geophysical Research: Space Physics*, *122*, 12,040–12,054. https://doi.org/10.1002/2017JA024475

Ebihara, Y., Ejiri, M., & Miyaoka, H. (1998). Coulomb lifetime of the ring current ions with time varying plasmasphere. *Earth, Planets and Space*, *50*(4), 371–382. https://doi.org/10.1186/BF03352123

Ebihara, Y., Yamada, M., Watanabe, S., & Ejiri, M. (2006). Fate of outflowing suprathermal oxygen ions that originate in the polar ionosphere. *Journal of Geophysical Research*, *111*, A04219. https://doi.org/10.1029/2005JA011403

Fernandes, P. A., Larsen, B. A., Thomsen, M. F., Skoug, R. M., Reeves, G. D., Denton, M. H., et al. (2017). The plasma environment inside geostationary orbit: A Van Allen Probes HOPE survey. *Journal of Geophysical Research: Space Physics*, *122*, 9207–9227. https://doi.org/10.1002/2017JA024160

Fok, M.-C., Kozyra, J. U., Nagy, A. F., & Cravens, T. E. (1991). Lifetime of ring current particles due to coulomb collisions in the plasmasphere. *Journal of Geophysical Research*, *96*(A5), 7861–7867. https://doi.org/10.1029/90JA02620

Fok, M.-C., Wolf, R. A., Spiro, R. W., & Moore, T. E. (2001). Comprehensive computational model of Earth's ring current. *Journal of Geophysical Research*, *106*(A5), 8417–8424. https://doi.org/10.1029/2000JA000235

Forster, D. R., Denton, M. H., Grande, M., & Perry, C. H. (2013). Inner magnetospheric heavy ion composition during high-speed stream-driven storms. *Journal of Geophysical Research: Space Physics*, *118*, 4066–4079. https://doi.org/10.1002/jgra.50292

Fu, S. Y., Zong, Q.-G., Wilken, B., & Pu, Z. Y. (2001). Temporal and spatial variation of the ion composition in the ring current. *Space Science Reviews*, *95*(1/2), 539–554. https://doi.org/10.1023/A:1005212906199

Funsten, H. O., Skoug, R. M., Guthrie, A. A., MacDonald, E. A., Baldonado, J. R., Harper, R. W., et al. (2013). Helium, Oxygen, Proton, and Electron (HOPE) mass spectrometer for the Radiation Belt Storm Probes mission. *Space Science Reviews*, *179*. https://doi.org/10.1007/s11214-013-9968-7

Gkioulidou, M., Ukhorskiy, A. Y., Mitchell, D. G., & Lanzerotti, L. J. (2016). Storm time dynamics of ring current protons: Implications for the long-term energy budget in the inner magnetosphere. *Geophysical Research Letters*, *43*, 4736–4744. https://doi.org/10.1002/2016GL068013

Greenspan, M. E., & Hamilton, D. C. (2002). Relative contributions of H+ and O+ to the ring current energy near magnetic storm maximum. *Journal of Geophysical Research*, *107*, A11S12. https://doi.org/10.1029/2001JA000155

Hirsch, K. L., Spence, H. E., & Onsager, T. G. (1996). Low altitude signatures of the plasma sheet: Model predictions of the local time dependence. *Journal of Geomagnetism and Geoelectricity*, *48*(5), 887–895. https://doi.org/10.5636/jgg.48.887

Horne, R. B., Thorne, R. M., Shprits, Y. Y., & Meredith, N. P. (2005). Wave acceleration of electrons in the Van Allen radiation belts. *Nature*, *437*(7056), 227–230. https://doi.org/10.1038/nature03939

Hsu, T. S., & McPherron, R. L. (2012). A statistical analysis of substorm associated tail activity. *Advances in Space Research*, *50*(10), 1317–1343. https://doi.org/10.1016/j.asr.2012.06.034

Jahn, J. M., Goldstein, J., Reeves, G. D., Fernandes, P. A., Skoug, R. M., Larsen, B. A., & Spence, H. E. (2017). The warm plasma composition in the inner magnetosphere during 2012–2015. *Journal of Geophysical Research: Space Physics*, *122*, 11,018–11,043. https://doi.org/10.1002/2017ja024183

Keesee, A., Goldstein, J., McComas, D. J., Scime, E. E., Spence, H. E., & Tallaksen, K. (2011). Remote observations of ion temperatures in the quiet time magnetosphere. *Geophysical Research Letters*, *38*, L03104. https://doi.org/10.1029/2010GL045987

Keika, K., Kistler, L. M., & Brandt, P. C. (2013). Energization of O+ ions in the Earth's inner magnetosphere and the effects on ring current buildup: A review of previous observations and possible mechanisms. *Journal of Geophysical Research: Space Physics*, *118*, 4441–4464. https://doi.org/10.1002/jgra.50371

Kistler, L. M., & Mouikis, C. G. (2016). The inner magnetosphere ion composition and local time distribution over a solar cycle. *Journal of Geophysical Research: Space Physics*, *121*, 2009–2032. https://doi.org/10.1002/2015JA021883

Kistler, L. M., Mouikis, C. G., Spence, H. E., Menz, A. M., Skoug, R. M., Funsten, H. O., et al. (2016). The source of O+ in the storm time ring current. *Journal of Geophysical Research: Space Physics*, *121*, 5333–5349. https://doi.org/10.1002/2015JA022204

Kivelson, M. G., & Spence, H. E. (1988). On the possibility of quasi-static convection in the quiet magnetotail. *Geophysical Research Letters*, *15*(13), 1541–1544. https://doi.org/10.1029/GL015i013p01541

Kletzing, C. A., Kurth, W. S., Acuna, M., MacDowall, R. J., Torbert, R. B., Averkamp, T., et al. (2013). The Electric and Magnetic Field Instrument Suite and Integrated Science (EMFISIS) on RBSP. *Space Science Reviews*, *179*(1-4), 127–181. https://doi.org/10.1007/s11214-013-9993-6

Kronberg, E. A., Grigorenko, E. E., Haaland, S. E., Daly, P. W., Delcourt, D. C., Luo, H., et al. (2015). Distribution of energetic oxygen and hydrogen in the near-Earth plasma sheet. *Journal of Geophysical Research: Space Physics*, *120*, 3415–3431. https://doi.org/10.1002/2014JA020882

Li, W., Shprits, Y. Y., & Thorne, R. M. (2007). Dynamic evolution of energetic outer zone electrons due to wave-particle interactions during storms. *Journal of Geophysical Research*, *112*, A10220. https://doi.org/10.1029/2007JA012368

Li, W., Thorne, R. M., Nishimura, Y., Bortnik, J., Angelopoulos, V., McFadden, J. P., et al. (2010). THEMIS analysis of observed equatorial electron distributions responsible for the chorus excitation. *Journal of Geophysical Research*, *115*, A00F11. https://doi.org/10.1029/2009JA014845

Liang, J., Donovan, E., Ni, B., Yue, C., Jiang, F., & Angelopoulos, V. (2014). On an energy-latitude dispersion pattern of ion precipitation potentially associated with magnetospheric EMIC waves. *Journal of Geophysical Research: Space Physics*, *119*, 8137–8160. https://doi.org/10.1002/2014JA020226

Liu, W. L., Fu, S. Y., Zong, Q., Pu, Z. Y., Yang, J., & Ruan, P. (2005). Variations of N+/O+ in the ring current during magnetic storms. *Geophysical Research Letters*, *32*(15), L1510. https://doi.org/10.1029/2005GL023038

Lorentzen, K. R., Blake, J. B., Inan, U. S., & Bortnik, J. (2001). Observations of relativistic electron microbursts in association with VLF chorus. *Journal of Geophysical Research*, *106*(A4), 6017–6027. https://doi.org/10.1029/2000JA003018

Lui, A. T. Y. (2003). Inner magnetospheric plasma pressure distribution and its local time asymmetry. *Geophysical Research Letters*, *30*(16), 1846. https://doi.org/10.1029/2003GL017596

Lui, A. T. Y., Spence, H. E., & Stern, D. P. (1994). Empirical modeling of the quiet time nightside magnetosphere. *Journal of Geophysical Research*, *99*(A1), 151. https://doi.org/10.1029/93JA02647

Maggiolo, R., & Kistler, L. M. (2014). Spatial variation in the plasma sheet composition: dependence on geomagnetic and solar activity. *Journal of Geophysical Research: Space Physics*, *119*, 2836–2857. https://doi.org/10.1002/2013JA019517

Mauk, B. H., Fox, N. J., Kanekal, S. G., Kessel, R. L., Sibeck, D. G., & Ukhorskiy, A. (2013). Science objectives and rationale for the Radiation Belt Storm Probes mission. *Space Science Reviews*, *179*(1-4), 3–27. https://doi.org/10.1007/s11214-012-9908-y

Meredith, N. P., Horne, R. B., Thorne, R. M., & Anderson, R. R. (2003). Favored regions for chorus-driven electron acceleration to relativistic energies in the Earth's outer radiation belt. *Geophysical Research Letters*, *30*, 1429. https://doi.org/10.1029/2003GL017698

Mitchell, D. G., Lanzerotti, L. J., Kim, C. K., Stokes, M., Ho, G., Cooper, S., et al. (2013). Radiation Belt Storm Probes Ion Composition Experiment (RBSPICE). *Space Science Reviews*, *179*. https://doi.org/10.1007/s1121 4-013-999 5-4

Ni, B., Li, W., Thorne, R. M., Bortnik, J., Ma, Q., Chen, L., et al. (2014). Resonant scattering of energetic electrons by unusual low-frequency hiss. *Geophysical Research Letters*, *41*, 1854–1861. https://doi.org/10.1002/2014GL059389

Reeves, G. D., Spence, H. E., Henderson, M. G., Morley, S. K., Friedel, R. H. W., Funsten, H. O., et al. (2013). Electron acceleration in the heart of the Van Allen radiation belts. *Science*, *341*(6149), 991–994. https://doi.org/10.1126/science.1237743

Sergeev, V. A., Sazhina, E. M., Tsyganenko, N. A., Lundblad, J. Å., & Søraas, F. (1983). Pitch-angle scattering of energetic protons in the magnetotail current sheet as the dominant source of their isotropic precipitation into the nightside ionosphere. *Planetary and Space Science*, *31*(10), 1147–1155. https://doi.org/10.1016/0032-0633(83)90103-4

Sharp, R. D., Lennartsson, W., Peterson, W. K., & Shelley, E. G. (1982). The origins of the plasma in the distant plasma sheet. *Journal of Geophysical Research: Space Physics*, *87*(A12), 10,420–10,424. https://doi.org/10.1029/JA087iA12p10420

Siscoe, G. L. (1983). Solar system magnetohydrodynamics (Vol. 104). Springer. https://doi.org/10.1007/978-94-009-7194-3_2

C:son Brandt, P., Demajistre, R., Roelof, E. C., Ohtani, S., Mitchell, D. G., & Mende, S. (2002). IMAGE/high-energy energetic neutral atom: Global energetic neutral atom imaging of the plasma sheet and ring current during substorms. *Journal of Geophysical Research*, *107*, 1454. https://doi.org/10.1029/2002JA009307

Spence, H., Reeves, G. D., Baker, D. N., Blake, J. B., Bolton, M., Bourdarie, S., et al. (2013). Science goals and overview of the Radiation Belt Storm Probes (RBSP) Energetic Particle, Composition, and Thermal Plasma (ECT) suite on NASA's Van Allen Probes mission. *Space Science Reviews*, *179*(1–4), 311–336. https://doi.org/10.1007/s11214-013-0007-5

Spence, H. E., & Kivelson, M. G. (1990). The variation of the plasma sheet polytropic index along the midnight meridian in a finite width tail. *Geophysical Research Letters*, *17*(5), 591–594. https://doi.org/10.1029/GL017i005p00591

Spence, H. E., & Kivelson, M. G. (1993). Contributions of the low-latitude boundary layer to the finite width magnetotail convection model. *Journal of Geophysical Research*, *98*(A9), 15487. https://doi.org/10.1029/93JA01531

Spence, H. E., Kivelson, M. G., & Walker, R. J. (1987). Static magnetic field models consistent with nearly isotropic plasma pressure. *Geophysical Research Letters*, *14*(8), 872–875. https://doi.org/10.1029/GL014i008p00872

Spence, H. E., Kivelson, M. G., Walker, R. J., & McComas, D. J. (1989). Magnetotail plasma pressures: Observations from 2.5 to 35 RE. *Journal of Geophysical Research*, *94*(A5), 5264–5272. https://doi.org/10.1029/JA094iA05p05264

Tao, X., Thorne, R. M., Li, W., Ni, B., Meredith, N. P., & Horne, R. B. (2011). Evolution of electron pitch-angle distributions following injection from the plasma sheet. *Journal of Geophysical Research*, *116*, A04229. https://doi.org/10.1029/2010JA016245

Thorne, R. M., Li, W., Ni, B., Ma, Q., Bortnik, J., Baker, D. N., et al. (2013). Evolution and slow decay of an unusual narrow ring of relativistic electrons near L ~3.2 following the September 2012 magnetic storm. *Geophysical Research Letters*, *40*, 3507–3511. https://doi.org/10.1002/grl.50627

Thorne, R. M., Li, W., Ni, B., Ma, Q., Bortnik, J., Chen, L., et al. (2013). Rapid local acceleration of relativistic radiation-belt electrons by magnetospheric chorus. *Nature*, *504*(7480), 411–414. https://doi.org/10.1038/nature12889

Tinsley, B. A. (1978). Effects of charge exchange involving H and H+ in the upper atmosphere. *Planetary and Space Science*, *26*(9), 847–853. https://doi.org/10.1016/0032-0633(78)90107-1

Wang, C. P., Gkioulidou, M., Lyons, L. R., Wolf, R. A., Angelopoulos, V., Nagai, T., et al. (2011). Spatial distributions of ions and electrons from the plasma sheet to the inner magnetosphere: Comparisons between THEMIS-Geotail statistical results and the Rice convection model. *Journal of Geophysical Research*, *116*, A11216. https://doi.org/10.1029/2011JA016809

Wang, C.-P., Yue, C., Zaharia, S., Xing, X., Lyons, L., Angelopoulos, V., et al. (2013). Empirical modeling of plasma sheet pressure and three-dimensional force-balanced magnetospheric magnetic field structure: 1. Observation. *Journal of Geophysical Research: Space Physics*, *118*, 6154–6165. https://doi.org/10.1002/jgra.50585

Wing, S., & Newell, P. (2002). Central plasma sheet ion properties as inferred from ionospheric observations. *Geophysical Research Letters*, *29*(9), 1307. https://doi.org/10.1029/2001GL013950

Wygant, J. R., Bonnell, J. W., Goetz, K., Ergun, R. E., Mozer, F. S., Bale, S. D., et al. (2013). The electric field and waves instruments on the Radiation Belt Storm Probes mission. *Space Science Reviews*, *179*(1–4), 183–220. https://doi.org/10.1007/s11214-013-0013-7

Yue, C., An, X., Bortnik, J., Ma, Q., Li, W., Thorne, R. M., et al. (2016). The relationship between the macroscopic state of electrons and the properties of chorus waves observed by the Van Allen Probes. *Geophysical Research Letters*, *43*, 7804–7812. https://doi.org/10.1002/2016GL070084

Yue, C., Bortnik, J., Chen, L., Ma, Q., Thorne, R. M., Reeves, G. D., & Spence, H. E. (2017). Transitional behavior of different energy protons based on Van Allen Probes observations. *Geophysical Research Letters*, *44*, 625–633. https://doi.org/10.1002/2016GL071324

Yue, C., Bortnik, J., Thorne, R. M., Ma, Q., An, X., Chappell, C. R., et al. (2017). The characteristic pitch angle distributions of 1 eV to 600 keV protons near the equator based on Van Allen Probes observations. *Journal of Geophysical Research: Space Physics*, *122*, 9464–9473. https://doi.org/10.1002/2017JA024421

Yue, C., Chen, L., Bortnik, J., Ma, Q., Thorne, R. M., Angelopoulos, V., et al. (2017). The characteristic response of whistler mode waves to interplanetary shocks. *Journal of Geophysical Research: Space Physics*, *122*, 10,047–10,057. https://doi.org/10.1002/2017JA024574

Yue, C., Li, W., Nishimura, Y., Zong, Q., Ma, Q., Bortnik, J., et al. (2016). Rapid enhancement of low-energy (<100 eV) ion flux in response to interplanetary shocks based on two Van Allen Probes case studies: Implications for source regions and heating mechanisms. *Journal of Geophysical Research: Space Physics*, *121*, 6430–6443. https://doi.org/10.1002/2016JA022808

Yue, C., Wang, C., Lyons, L., Wang, Y., Hsu, T., Henderson, M., et al. (2015). A 2-D empirical plasma sheet pressure model for substorm growth phase using the support vector regression machine. *Journal of Geophysical Research: Space Physics*, *120*, 1957–1973. https://doi.org/10.1002/2014JA020787

Yue, C., Wang, C.-P., Lyons, L., Liang, J., Donovan, E. F., Zaharia, S. G., & Henderson, M. (2014). Current sheet scattering and ion isotropic boundary under 3-D empirical force-balanced magnetic field. *Journal of Geophysical Research: Space Physics*, *119*, 8202–8211. https://doi.org/10.1002/2014JA020172

Yue, C., Zong, Q., Wang, Y., Vogiatzis, I. I., Pu, Z., Fu, S., & Shi, Q. (2011). Inner magnetosphere plasma characteristics in response to interplanetary shock impacts. *Journal of Geophysical Research*, *116*, A11206. https://doi.org/10.1029/2011JA016736

Yue, C., Zong, Q. G., Zhang, H., Wang, Y. F., Yuan, C. J., Pu, Z. Y., et al. (2010). Geomagnetic activity triggered by interplanetary shocks. *Journal of Geophysical Research*, *115*, A00I05. https://doi.org/10.1029/2010JA015356

Zhao, H., Zhao, H., Li, X., Baker, D. N., Fennell, J. F., Blake, J. B., et al. (2015). The evolution of ring current ion energy density and energy content during geomagnetic storms based on Van Allen Probes measurements. *Journal of Geophysical Research: Space Physics*, *120*, 7493–7511. https://doi.org/10.1002/2015JA021533